

**1      A direct comparison between field-measured**

**2      and sensor-based estimates of soil carbon**

**3      dioxide flux across six National Ecological**

**4      Observatory Network sites enabled by the**

**5      neonSoilFlux R package**

**6      John Zobitz<sup>1</sup>      Ed Ayres<sup>2</sup>      Zoey Werbin<sup>3</sup>      Ridwan Abdi<sup>1</sup>**

**7      Natalie Ashburner-Wright<sup>4</sup>      Lillian Brown<sup>4</sup>**

**8      Ryan Frink-Sobierajski<sup>4</sup>      Lajntxiag Lee<sup>1</sup>      Dijonë Mehmeti<sup>1</sup>**

**9      Christina Tran<sup>4</sup>      Ly Xiong<sup>1</sup>      Naupaka Zimmerman<sup>4</sup>**

**10     <sup>1</sup> Augsburg University, 2211 Riverside Avenue, Minneapolis, MN 55454**

**11     <sup>2</sup> National Ecological Observatory Network, 1685 38th Street, Suite 100, Boulder, CO 80301**

**12     <sup>3</sup> Boston University, 5 Cummington Street, Boston, MA 02215**

**13     <sup>4</sup> University of San Francisco, 2130 Fulton Street, San Francisco, CA 94117**

<sup>14</sup> **Acknowledgments**

<sup>15</sup> JZ acknowledges Kathleen O'Rourke for code development. NZ thanks technical staff at  
<sup>16</sup> USF for support with field gear assembly and shipping. We thank the NEON field staff  
<sup>17</sup> and assignable assets teams for facilitating each of the six NEON site visits. We are grateful  
<sup>18</sup> to LI-COR technical staff for helpful discussions about optimal sampling methods. This work  
<sup>19</sup> was supported by NSF DEB grant #2017829 awarded to JZ, and NSF DEB grant #2017860  
<sup>20</sup> awarded to NZ.

<sup>21</sup> **Conflict of Interest Statements**

<sup>22</sup> None of the authors have a financial, personal, or professional conflict of interest related to  
<sup>23</sup> this work.

<sup>24</sup> **Author Contributions**

<sup>25</sup> Conceptualization: JZ, NZ; Methodology: EA, JZ, NZ; Software: JZ, NZ, ZW, E A, DM, RA,  
<sup>26</sup> LX, LL; Validation: JZ, NZ; Formal Analysis: JZ, NZ, DM, RA, LX, LL; Investigation: JZ,  
<sup>27</sup> NZ, RF-S, CT, NA-W, LB; Resources: JZ, NZ; Data curation: JZ, NZ, DM, LX; Writing  
<sup>28</sup> – original draft: JZ, NZ; Writing – review and editing: JZ, NZ, ZW, EA, CT, DM, LX,;  
<sup>29</sup> Visualization: JZ, NZ, DM, RA, LX; Supervision: JZ; NZ; Project Administration: JZ; NZ;  
<sup>30</sup> Funding Acquisition: JZ; NZ

<sup>31</sup> **Data Availability**

<sup>32</sup> Data available from the Zenodo LINK <http://dx.doi.org/10.5061/dryad.41qh7> (Kiere & Drummond 2016)."

<sup>34</sup> **1 Abstract**

<sup>35</sup> A key component of constraining the uncertainty of the terrestrial carbon sink is quantification  
<sup>36</sup> of terrestrial soil carbon fluxes, which vary across time and ecosystem type. One method for  
<sup>37</sup> the estimation of these fluxes and their associated uncertainties is the flux gradient method,  
<sup>38</sup> which can be calculated via a variety of existing approaches. Robust estimation of soil carbon  
<sup>39</sup> fluxes on a sub-daily level requires measurements of soil CO<sub>2</sub> concentration, water content,  
<sup>40</sup> temperature, and other environmental measurements and soil properties. These data are  
<sup>41</sup> publicly available from the National Ecological Observatory Network at sites spanning a range  
<sup>42</sup> of 20 different ecoclimatic domains across the continental United States, Puerto Rico, Alaska,  
<sup>43</sup> and Hawai'i. We present an R software package (`neonSoilFlux`) that acquires NEON soil  
<sup>44</sup> environmental data and computes soil carbon flux at a half-hourly time step at a user-specified  
<sup>45</sup> NEON site and month in a tidy data format. To validate the computed fluxes, we visited six  
<sup>46</sup> focal NEON sites and measured soil carbon fluxes using a closed-dynamic chamber approach.  
<sup>47</sup> The validation confirmed that a primary challenge in reducing soil carbon flux uncertainty is  
<sup>48</sup> correctly characterizing diffusivity and soil water content across the soil profile. Outputs from  
<sup>49</sup> the `neonSoilFlux` package contribute to existing databases of soil carbon flux measurements,  
<sup>50</sup> providing near real-time estimates of a critical component of the terrestrial carbon cycle.

<sup>51</sup> **1.1 Keywords**

<sup>52</sup> Soil carbon, carbon dioxide, flux gradient, carbon cycle, field validation, soil respiration, ecosys-  
<sup>53</sup> tem variability, diffusion

<sup>54</sup> **2 Data for peer review**

<sup>55</sup> Anonymous data and code for peer review is available here: [LINK](#)

<sup>56</sup> **3 Introduction**

<sup>57</sup> Soils contain the largest reservoir of terrestrial carbon (Jobbágy & Jackson, 2000). A critical  
<sup>58</sup> component of this reservoir is soil organic matter, the accumulation of which is influenced  
<sup>59</sup> by biotic factors such as above-ground plant inputs (Jackson et al., 2017). These inputs in  
<sup>60</sup> turn are influenced by environmental factors such as growing season length, temperature, and  
<sup>61</sup> moisture (Desai et al., 2022), which also affect the breakdown of soil organic matter and its  
<sup>62</sup> return to the atmosphere. Across heterogeneous terrestrial landscapes, the interplay between  
<sup>63</sup> these biotic and abiotic factors influence the size of the soil contribution to the terrestrial  
<sup>64</sup> carbon sink (Friedlingstein et al., 2023). However, the heterogeneity of these processes across  
<sup>65</sup> diverse ecosystems in the context of rapid environmental change leads to large uncertainty in  
<sup>66</sup> the magnitude of this sink in the future, and thus a pressing need to quantify changes in soil  
<sup>67</sup> carbon pools and fluxes across scales.

<sup>68</sup> Ecological observation networks such as the United States' National Ecological Observatory  
<sup>69</sup> Network (NEON) and others (e.g. FLUXNET or the Integrated Carbon Observation System)  
<sup>70</sup> present a significant advancement in the nearly continuous observation of biogeochemical pro-  
<sup>71</sup> cesses at the continental scale. Notably, at 47 terrestrial sites across the continental United  
<sup>72</sup> States, NEON provides half-hourly measurements of soil CO<sub>2</sub> concentration, temperature,  
<sup>73</sup> and moisture at different vertical depths. Each of these NEON sites also encompasses mea-  
<sup>74</sup> surements of the cumulative sum of all ecosystem carbon fluxes in an airshed using the eddy  
<sup>75</sup> covariance technique (Balderuppi, 2014). Soil observations provided by NEON are on the same

76 timescale and standardized with eddy covariance measurements from FLUXNET. These types  
77 of nearly continuous observational data (NEON and FLUXNET) can be used to reconcile dif-  
78 ferences between model-derived or data-estimated components of ecosystem carbon flux (Jian  
79 et al., 2022; Luo et al., 2011; Phillips et al., 2017; J. Shao et al., 2015; P. Shao et al., 2013;  
80 Sihi et al., 2016).

81 Estimated or observed soil carbon fluxes are a key metric for understanding change in soil  
82 carbon pools over time (Bond-Lamberty et al., 2024). A soil carbon flux to the atmosphere  
83 ( $F_S$ , units  $\mu\text{mol m}^{-2} \text{s}^{-1}$ ), represents the aggregate process of transfer of soil  $\text{CO}_2$  to the  
84 atmosphere from physical and biological processes (e.g. diffusion and respiration). Soil carbon  
85 fluxes can be assumed to encompass soil carbon respiration from autotrophic or heterotrophic  
86 sources (Davidson et al., 2006), typically assumed to be static across the soil biome and  
87 modeled with a exponential  $Q_{10}$  paradigm (Bond-Lamberty et al., 2004; Chen & Tian, 2005;  
88 Hamdi et al., 2013).

89 One method by which  $F_S$  is measured in the field is through the use of soil chambers in a closed,  
90 well-mixed system (Norman et al., 1997) with headspace trace gas concentrations measured  
91 with an infrared gas analyzer (IRGA).  $F_S$  can also be estimated from soil  $\text{CO}_2$  measurements  
92 at different depths in the soil using the flux-gradient method (Maier & Schack-Kirchner, 2014).  
93 This method is an approach that uses conservation of mass to calculate flux at a vertical soil  
94 depth  $z$  at steady state by applying Fick's law of diffusion. A simplifying assumption for the  
95 flux-gradient method is that there is no mass transfer in the other spatial dimensions  $x$  and  $y$   
96 (Maier & Schack-Kirchner, 2014). The diffusivity profile, a key component of this calculation,  
97 varies across the soil depth as a function of soil temperature, soil volumetric water content,  
98 atmospheric air pressure, and soil bulk density (Millington & Shearer, 1971; Moldrup et al.,  
99 1999; Sallam et al., 1984).

100 Databases such as the Soil Respiration Database (SRDB) or the Continuous Soil Respiration

101 Database (COSORE) add to the growing network of resources for making collected observa-  
102 tions of soil fluxes available to other workers (Bond-Lamberty, 2018; Bond-Lamberty et al.,  
103 2020; Bond-Lamberty & Thomson, 2010; Jian et al., 2021; Jiang et al., 2024). However, these  
104 databases currently encompass primarily direct soil measurements of fluxes (i.e. those using  
105 methods like the closed-chamber method described above). Currently, NEON provides all  
106 measurements to calculate  $F_S$  from Fick's law, but soil flux as a derived data product was  
107 descoped from the initial network launch due to budget constraints (Berenbaum et al., 2015).  
108 Deriving estimates of  $F_S$  using continuous sensor data across NEON sites thus represents a  
109 high priority.

110 This study describes an R software package, `neonSoilFlux`, that can be used to derive a  
111 standardized estimate of  $F_S$  at all terrestrial NEON sites. After calculating these flux estimates,  
112 we then validated them against direct chamber-based field observations of soil carbon dioxide  
113 flux from a subset of terrestrial NEON sites spanning six states.

114 Key objectives of this study are to:

- 115 1. Apply the flux-gradient method to estimate soil CO<sub>2</sub> flux from continuous sensor mea-  
116 surements across NEON sites.
- 117 2. Benchmark estimated soil carbon fluxes against field measurements (e.g. direct chamber  
118 measurements of soil flux).
- 119 3. Identify sources of error in the flux-gradient approach across diverse sites in order to  
120 guide future work.

<sub>121</sub> **4 Materials and Methods**

<sub>122</sub> **4.1 Field methods**

<sub>123</sub> **4.1.1 Focal NEON Sites**

<sub>124</sub> In order to acquire field data to validate model predictions of flux, we selected six terrestrial  
<sub>125</sub> NEON sites for analysis. We conducted field measurement campaigns at these sites, which  
<sub>126</sub> span a range of environmental gradients and terrestrial domains (Table 1). SJER, SRER, and  
<sub>127</sub> WREF were visited during May and June of 2022, and WOOD, KONZ, and UNDE during  
<sub>128</sub> May and June of 2024.

<sub>129</sub> Over the course of two field campaigns in 2022 and 2024, we conducted week-long visits at  
<sub>130</sub> each site. In consultation with NEON field staff, we first selected a specific plot in the soil  
<sub>131</sub> sampling array to maximize the concurrent availability of sensor data.

<sub>132</sub> **4.1.2 Soil collar placement**

<sub>133</sub> Either one (2022 sampling campaign) or two (2024 sampling campaign) PVC soil collars (20.1  
<sub>134</sub> cm inside diameter) were installed in close proximity to the permanent NEON soil sensors at  
<sub>135</sub> each site (Figure 1). The soil plot where measurements were taken was chosen at each site  
<sub>136</sub> in consultation with NEON staff to maximize likelihood of quality soil sensor measurements  
<sub>137</sub> during the duration of the IRGA measurements at each site. After installation, collar(s) were  
<sub>138</sub> left to equilibrate for approximately 24 hours prior to measurements being taken.

<sup>139</sup> **4.1.3 Infrared gas analyzer measurements of soil CO<sub>2</sub> flux**

<sup>140</sup> In 2022, we then made measurements of flux on an hourly interval for 8 hours each day.  
<sup>141</sup> Measurements were taken from roughly 8 am to 4 pm, with the time interval selected to  
<sup>142</sup> capture the majority of the diurnal gradient of soil temperature each day. These measurements  
<sup>143</sup> were made using a LI-6800 infrared gas analyzer instrument (LI-COR Environmental, Lincoln,  
<sup>144</sup> NE) fitted with a soil chamber attachment (attachment 6800-09). In 2024, we again used  
<sup>145</sup> the same LI-6800 instrument, but made half-hourly measurements over an approximately 8  
<sup>146</sup> hour period. In addition, we also installed a second collar and used a second instrument, an  
<sup>147</sup> LI-870 CO<sub>2</sub> IRGA, connected to an automated robotic chamber (LI-COR chamber 8200-104)  
<sup>148</sup> controlled by an LI-8250 multiplexer, to make automated measurements. The multiplexer was  
<sup>149</sup> configured to take half-hourly measurements 24 hours a day for the duration of our sampling  
<sup>150</sup> bout at each site. Each instrument was paired with a soil temperature and moisture probe  
<sup>151</sup> (Stevens HydraProbe, Stevens Water, Portland, OR) that was used to make soil temperature  
<sup>152</sup> and moisture measurements concurrent with the CO<sub>2</sub> flux measurements. Chamber volumes  
<sup>153</sup> were set by measuring collar offsets at each site. System checks were conducted daily for the  
<sup>154</sup> LI-6800 and weekly for the LI-8250. Instruments were factory calibrated before each field  
<sup>155</sup> season.

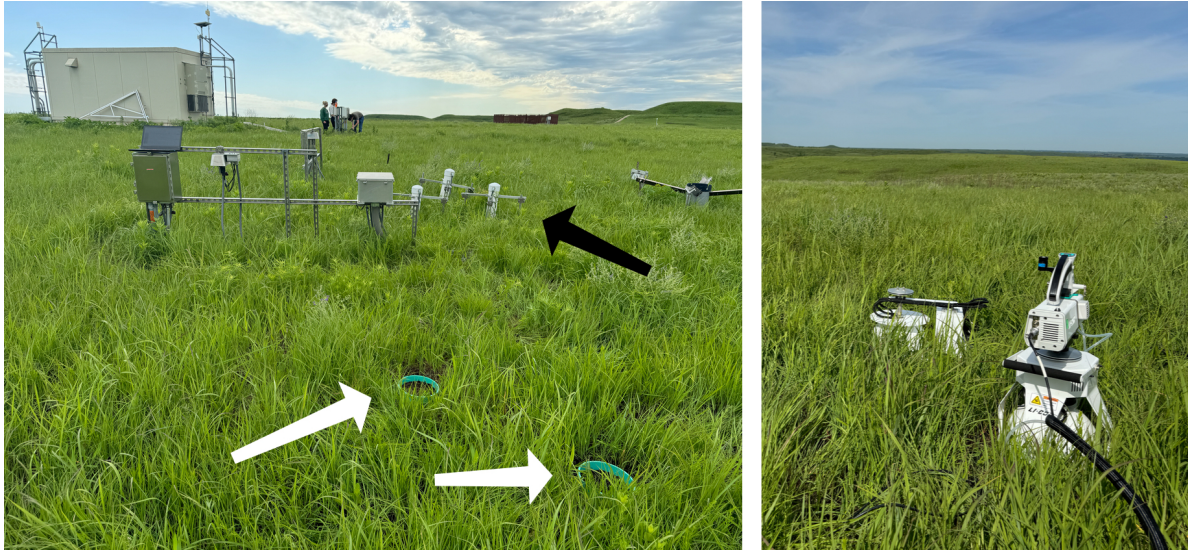


Figure 1: Spatial layout of field sampling using a closed-dynamic chamber setup at a representative NEON site (KONZ). Left image shows collars (white arrows) and permanent soil sensor installation (black arrow) and right image shows the LI-6800 (foreground) and LI-8200-104 (background) instruments placed on the collars.

Table 1: Listing of NEON sites studied for field work and analysis.  $\overline{T_S}$ : average soil temperature during field measurements.  $\overline{SWC}$ : average soil water content during field measurements. Soil plot refers to the particular location in the soil sensor array (denoted as HOR by NEON) where field measurements were made.

Site (NEON site ID)	Location	Ecosystem type	Mean annual tempera- ture	$\overline{T_S}$ (°)	Mean annual precipita- tion	$\overline{SWC}$ (%)	Field measure- ment dates	Soil plot
Santa	31.91068,	Shrubland	19.3°C	47.6°	346 mm	4.0%	29 May	004
Rita	-						2024 - 01	
Experi- mental Range (SRER)	110.83549						June 2024	

Table 1: Listing of NEON sites studied for field work and analysis.  $\bar{T}_S$ : average soil temperature during field measurements.  $\bar{SWC}$ : average soil water content during field measurements. Soil plot refers to the particular location in the soil sensor array (denoted as HOR by NEON) where field measurements were made.

Site (NEON site ID)	Location	Ecosystem type	Mean annual tempera- ture	$\bar{T}_S$ (°)	Mean annual precipita- tion	$\bar{SWC}$ (%)	Field measure- ment dates	Soil plot
San Joaquin Experimental Range (SJER)	37.10878, -	Oak woodland	16.4°C	41.7°	540 mm	1.2%	01 June 2022 - 04	005
Experi- mental Range (SJER)	119.73228						June 2022	
Wind River Experimental Forest (WREF)	45.82049, -	Evergreen forest	9.2°C	15.3°	2225 mm	27.2%	07 June 2022 - 09	001
Chase Lake Wildlife Refuge (WOOD)	121.95191 47.1282, - 99.241334	Restored prairie	4.9°C	14.9°	495 mm	14.9%	03 June 2024 - 09	001
National Biological Station (KONZ)		grassland					June 2024	
Konza Prairie	39.100774, -	Tallgrass Prairie	12.4°C	23.4°	870 mm	23.4%	29 May 2024 - 01	001
	96.563075						June 2024	

Table 1: Listing of NEON sites studied for field work and analysis.  $\bar{T}_S$ : average soil temperature during field measurements.  $\bar{SWC}$ : average soil water content during field measurements. Soil plot refers to the particular location in the soil sensor array (denoted as HOR by NEON) where field measurements were made.

Site (NEON site ID)	Location	Ecosystem type	Mean annual tempera- ture	$\bar{T}_S$ (°)	Mean annual precipita- tion	$\bar{SWC}$ (%)	Field measure- ment dates	Soil plot
University of Notre Dame Environ- mental Research Center (UNDE)	46.23391, - 89.537254	Deciduous forest	4.3°	13.0°	802 mm	13.0%	22 May 2024 - 25 May 2024	004

#### **4.1.4 Post-collection processing of field data**

We used LI-COR SoilFluxPro software (v 5.3.1) to assess the data after collection and to inform sampling parameters. We checked appropriateness of dead band and measurement durations using built-in evaluation tools. Based on this, the deadband period was set for 30-40 seconds, depending on the site, and the measurement duration was 180 seconds with a 30 second pre-purge and a 30 second post-purge at most sites, and a 90 sec pre- and post-purge at sites with higher humidity due to recent precipitation events. We also assessed the  $R^2$  of linear and exponential model fits to measured  $\text{CO}_2$  to verify measurement quality.

164 **4.2 neonSoilFlux R package**

165 We developed an R package (`neonSoilFlux`; <https://CRAN.R-project.org/package=neonSoilFlux>)  
166 to compute half-hourly soil carbon fluxes and uncertainties from NEON data. The objective  
167 of the `neonSoilFlux` package is a unified workflow (Figure 2) for soil data acquisition and  
168 analysis that supplements the existing data acquisition R package `neonUtilities` (LINK TO  
169 BE ADDED AFTER PEER REVIEW).

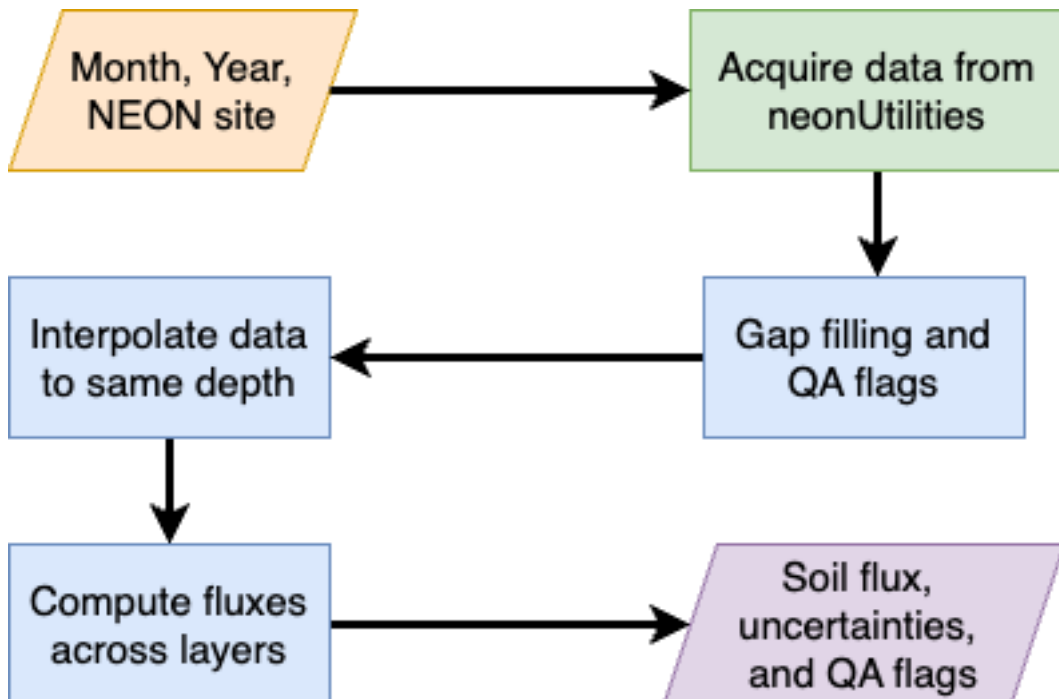


Figure 2: Diagram of `neonSoilFlux` R package. For a given month, year, and NEON site (orange parallelogram), the package acquires all relevant data to compute  $F_S$  using the `neonUtilities` R package (green rectangle). Data are gap-filled according to reported QA flags and interpolated to the same measurement depth before computing the soil flux, uncertainties, and final QA flags (blue rectangles). The package reports the associated soil flux, uncertainties, and quality assurance (QA) flags for the user (purple parallelogram).

170 At a given NEON observation there are five replicate soil plots, each with measurements of  
171 soil  $\text{CO}_2$  concentration, soil temperature, and soil moisture at different depths (Figure 3). The

172 `neonSoilFlux` package acquires measured soil water content (National Ecological Observatory  
 173 Network (NEON), 2024e), soil CO<sub>2</sub> concentration (National Ecological Observatory Network  
 174 (NEON), 2024b), barometric pressure from the nearby tower (National Ecological Observa-  
 175 tory Network (NEON), 2024a), soil temperature (National Ecological Observatory Network  
 176 (NEON), 2024d), and soil properties (e.g. bulk density) (National Ecological Observatory Net-  
 177 work (NEON), 2024c). The static soil properties were collected from a nearby soil pit during  
 178 site characterization and are assumed to be constant at each site.

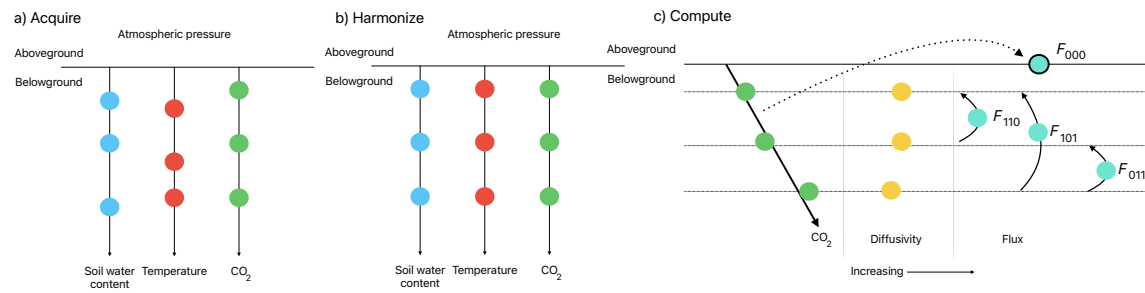


Figure 3: Model diagram for data workflow for the `neonSoilFlux` R package. a) Acquire: Data are obtained from given NEON location and horizontal sensor location, which includes soil water content, soil temperature, CO<sub>2</sub> concentration, and atmospheric pressure. All data are screened for quality assurance; if gap-filling of missing data occurs, it is flagged for the user. b) Any belowground data are then harmonized to the same depth as CO<sub>2</sub> concentrations using linear regression. c) The flux across a given depth is computed via Fick's law, denoted with  $F_{ijk}$ , where  $i$ ,  $j$ , or  $k$  are either 0 or 1 denoting the layers the flux is computed across ( $i$  = closest to surface,  $k$  = deepest).  $F_{000}$  represents a flux estimate where the gradient  $dC/dz$  is the slope of a linear regression of CO<sub>2</sub> with depth.

179 The workflow to compute a value of  $F_S$  with `neonSoilFlux` consists of three primary steps,  
 180 illustrated in Figure 3. First, NEON data are acquired for a given site and month via the  
 181 `neonUtilities` R package (yellow parallelogram and green rectangle in Figure 2 and Panel a  
 182 in Figure 3). Acquired environmental data can be exported to a comma separated value file  
 183 for additional analysis. Quality assurance (QA) flags are reported as an indicator variable.  
 184 The second step is harmonizing the data to compute soil fluxes across soil layers. This step

185 consists of three different actions (blue rectangles in Figure 2 and Panel b in Figure 3). If a  
186 given observation by NEON is reported as not passing a quality assurance check, we applied  
187 a gap filling method to replace that measurement with its monthly mean at that same depth  
188 (Section 4.2.1). Belowground measurements of soil water and soil temperature are then inter-  
189 polated to the same depth as soil CO<sub>2</sub> measurements. The diffusivity (Section 4.2.2) and soil  
190 flux across different soil layers (Section 4.2.3) are then computed.

191 The third and final step is computing a surface soil flux through extrapolation to the sur-  
192 face (purple parallelogram in Figure 2 and Panel c in Figure 3). Uncertainty on a soil flux  
193 measurement is computed through quadrature. An aggregate quality assurance (QA) flag  
194 for each environmental measurement is also reported, representing if any gap-filled measure-  
195 ments were used in the computation of a soil flux. Within the soil flux-gradient method,  
196 several different approaches can be used to derive a surface flux (Maier & Schack-Kirchner,  
197 2014); the `neonSoilFlux` package reports four different possible values for soil surface flux  
198 (Section 4.2.3).

#### 199 4.2.1 Gap-filling routine

200 NEON reports QA flags as a binary value for a given measurement and half-hourly time inter-  
201 val. We replaced any flagged measurements at a location's spatial depth  $z$  with a bootstrapped  
202 sample of the monthly mean for all un-flagged measurements for that month. These measure-  
203 ments are represented by the vector  $\mathbf{m}$ , standard errors  $\sigma$ , and the 95% confidence interval  
204 (the so-called expanded uncertainty, Farrance & Frenkel (2012))  $\epsilon$ . All of these vectors have  
205 length  $M$ . We have that  $\vec{\sigma}_i \leq \vec{\epsilon}_i$ . We define the bias as  $\mathbf{b} = \sqrt{\epsilon^2 - \sigma^2}$ .

206 We generate a vector of bootstrap samples of the distribution of the monthly mean  $\bar{m}$  and  
207 monthly standard error  $\bar{\sigma}$  the following ways:

- 208 1. Randomly sample from the uncertainty and bias independently:  $\sigma_j$  and the bias  $\mathbf{b}_k$  (not  
 209 necessarily the same sample).
- 210 2. Generate a vector  $\mathbf{n}$  of length  $N$ , where  $\mathbf{n}_i$  is a random sample from a normal distribution  
 211 with mean  $m_i$  and standard deviation  $\sigma_j$ . Since  $M < N$ , values from  $\mathbf{m}$  will be reused.
- 212 3. With these  $N$  random samples,  $\bar{y}_i = \vec{x} + \vec{b}_k$  and  $s_i$  is the sample standard deviation of  $\vec{x}$ .  
 213 We expect that  $s_i \approx \vec{\sigma}_j$ .
- 214 4. The reported monthly mean and standard deviation are then computed  $\bar{\bar{y}}$  and  $\bar{s}$ . Measurements and uncertainties that did not pass the QA check are then substituted with  
 215  $\bar{\bar{y}}$  and  $\bar{s}$ .

217 This gap-filling method described here provides a consistent approach for each data stream,  
 218 however we recognize that other gap-filling alternatives may be warranted for longer-term gaps  
 219 (e.g. such as correlations with other NEON measurement levels and soil plots), or measure-  
 220 ment specific gap-filling routines. We discuss the effect of gap-filling on our measurements in  
 221 Section 6.

222 **4.2.2 Soil diffusivity**

223 Soil diffusivity  $D_a$  at a given measurement depth is the product of the diffusivity in free air  
 224  $D_{a,0}$  ( $\text{m}^2 \text{ s}^{-1}$ ) and the tortuosity  $\xi$  (no units) (Millington & Shearer, 1971).

225 We compute  $D_{a,0}$  with Equation 1:

$$D_{a,0} = 0.0000147 \cdot \left( \frac{T_i + 273.15}{293.15} \right)^{1.75} \cdot \left( \frac{P}{101.3} \right) \quad (1)$$

226 where  $T_i$  is soil temperature ( $^{\circ}\text{C}$ ) at depth  $i$  (National Ecological Observatory Network  
 227 (NEON), 2024d) and  $P$  surface barometric pressure (kPa) (National Ecological Observatory  
 228 Network (NEON), 2024a).

229 Previous studies by Sallam et al. (1984) and Tang et al. (2003) demonstrated the sensitivity  
 230 of modeled  $F_S$  depending on the tortuosity model used to compute diffusivity. At low soil  
 231 water content, the choice of tortuosity model may lead to order of magnitude differences in  
 232  $D_a$ , which in turn affect modeled  $F_S$ . The `neonSoilFlux` package uses two different models  
 233 for  $\xi$ , representing the extremes reported in Sallam et al. (1984). The first approach uses the  
 234 Millington-Quirk model for diffusivity, Equation 2 (Millington & Shearer, 1971):

$$\xi = \frac{(\phi - SWC_i)^{10/3}}{\phi^2} \quad (2)$$

235 In Equation 2,  $SWC$  is the soil water content at depth  $i$  (National Ecological Observatory  
 236 Network (NEON), 2024e) and  $\phi$  is the porosity (Equation 3), which in turn is a function of  
 237 soil physical properties (National Ecological Observatory Network (NEON), 2024c):

$$\phi = \left(1 - \frac{\rho_s}{\rho_m}\right) (1 - f_V) \quad (3)$$

238 In Equation 3,  $\rho_m$  is the particle density of mineral soil ( $2.65 \text{ g cm}^{-3}$ ),  $\rho_s$  the soil bulk density  
 239 ( $\text{g cm}^{-3}$ ) excluding coarse fragments greater than 2 mm (National Ecological Observatory  
 240 Network (NEON), 2024c). The term  $f_V$  is a site-specific value that accounts for the proportion  
 241 of soil fragments between 2-20 mm. Soil fragments greater than 20 mm were not estimated  
 242 due to limitations in the amount of soil that can be analyzed (National Ecological Observatory  
 243 Network (NEON), 2024c). We assume there are no pores within rocks.

<sup>244</sup> The second approach to calculate  $\xi$  is the Marshall model (Marshall, 1959), where  $\xi = \phi^{1.5}$ ,  
<sup>245</sup> with  $\phi$  defined from Equation 3.

<sup>246</sup> **4.2.3 Soil flux computation**

<sup>247</sup> We applied Fick's law (Equation 4) to compute the soil flux  $F_{ij}$  ( $\mu\text{mol m}^{-2} \text{s}^{-1}$ ) across two  
<sup>248</sup> soil depths  $i$  and  $j$ :

$$F_{ij} = -D_a \frac{dC}{dz} \quad (4)$$

<sup>249</sup> where  $D_a$  is the diffusivity ( $\text{m}^2 \text{s}^{-1}$ ) and  $\frac{dC}{dz}$  is the gradient of CO<sub>2</sub> molar concentration  
<sup>250</sup> ( $\mu\text{mol m}^{-3}$ , so the gradient has units of  $\mu\text{mol m}^{-3} \text{m}^{-1}$ ). The soil surface flux is theoretically  
<sup>251</sup> defined by applying Equation 4 to measurements collected at the soil surface and directly  
<sup>252</sup> below the surface. Measurements of soil temperature, soil water content, and soil CO<sub>2</sub> molar  
<sup>253</sup> concentration across the soil profile allow for application of Equation 4 across different soil  
<sup>254</sup> depths. Each site had three measurement layers, so we denote the flux between which two  
<sup>255</sup> layers as a three-digit subscript  $F_{ijk}$  with indicator variables  $i$ ,  $j$ , and  $k$  indicate if a given  
<sup>256</sup> layer was used (written in order of increasing depth), according to the following:

- <sup>257</sup> •  $F_{000}$  is a surface flux estimate using the intercept of the linear regression of  $D_a$  with  
<sup>258</sup> depth and the slope from the linear regression of CO<sub>2</sub> with depth (which represents  $\frac{dC}{dz}$   
<sup>259</sup> in Fick's Law). Tang et al. (2003) used this approach to compute fluxes in an oak-grass  
<sup>260</sup> savannah.
- <sup>261</sup> •  $F_{110}$ ,  $F_{011}$  are fluxes across the two most shallow layers and two deepest layers respec-  
<sup>262</sup> tively. The diffusivity used in Fick's Law is always at the deeper measurement layer.

When used as a surface flux estimate we assume CO<sub>2</sub> remains constant above this flux depth.

- $F_{101}$  is a surface flux estimate using linear extrapolation using concentration measurements between the shallowest and deepest measurement layer. Hirano et al. (2003) and Tang et al. (2005) used an approach similar to  $F_{101}$  in a temperate deciduous broadleaf forest and ponderosa pine forest respectively.

Uncertainty in all  $F_{ijk}$  is computed through quadrature (Taylor, 2022).

### 4.3 Post processing evaluation

Following collection of field measurements and calculation of the soil fluxes from `neonSoilFlux` package, we compared measured  $F_S$  based on closed-dynamic chamber measurements with the LI-COR instruments to a given soil flux calculation from `neonSoilFlux` for each site and flux computation method. Statistics included the associated R<sup>2</sup> value, root mean squared error (RMSE), and signal to noise ratio (SNR), defined as the ratio of a modeled soil flux ( $F_{ijk}$ ) from `neonSoilFlux` to its quadrature uncertainty ( $\sigma_{ijk}$ ).

We observed that the range of values (e.g.  $F_{ijk} \pm \sigma_{ijk}$ ) was much larger than the measured field flux. We evaluated  $|F_S - F_{ijk}| < (1 - \epsilon)\sigma_{ijk}$ , where  $F_S$  is a measured field soil flux from the LI-COR 6800 (as the LI-COR 870/8250 was used at only three sites in 2024 but the 6800 was used at all sites in both years). The parameter  $\epsilon$  was an uncertainty reduction factor to evaluate how much the quadrature uncertainty could be reduced while maintaining precision between modeled  $F_{ijk}$  and measured  $F_S$ .

Finally, for a half-hourly interval we also computed a *post hoc*  $D_a$  using the LI-COR flux along with the CO<sub>2</sub> surface gradient reported by NEON using the measurement levels closest to the surface.

286 **5 Results**

287 Our overall goal was to design and validate an R package to estimate soil carbon dioxide  
288 fluxes fluxes across terrestrial NEON sites using the flux gradient method. Validation of the  
289 approach was based on comparison of estimated fluxes to field measurements made at six  
290 focal sites. We first present our field measurement results, then the concordance between the  
291 modeled and measured results, and lastly assess the factors that influenced the success of the  
292 modeled approach at a given site.

293 **5.1 Field measurements**

294 We visited six NEON sites in the summers of 2022 and 2024. Using a closed-dynamic chamber  
295 approach, we quantified soil carbon dioxide fluxes over the course of a week at each site. The  
296 sites we visited ranged substantially in both their annual average temperature and precipitation  
297 as well as their biome type (Table 2). These differences also influenced the wide range of  
298 observed flux rates across sites. We used a LI-6800 to take manual hourly measurements at  
299 the sites we visited in 2022 (SRER, SJER, WREF) and half-hourly manual measurements for  
300 the sites we visited in 2024 (UNDE, KONZ, WOOD). In 2024 we also used an automated  
301 chamber system (LI-870/LI-8250) to take half-hourly measurements 24 hours a day, thereby  
302 also capturing nighttime fluxes in addition to the daytime fluxes also measured with the LI-  
303 6800.

304 **5.2 Concordance between modelled and measured soil CO<sub>2</sub> flux**

305 The timeseries of the measured fluxes from the LI-COR 6800 and 870/8250 were compared  
306 to modeled soil fluxes from the `neonSoilFlux` R package (Figure 4). We also assessed year-

Table 2: Summary of measured soil characteristics and flux results from field measurements across six NEON sites using a LI-COR 6800 (LI-870/8250 measurements omitted to enable direct comparability) via the closed-dynamic chamber method. Numeric values for soil CO<sub>2</sub> flux, soil temperature, and volumetric soil water content (VSWC) are the mean and standard deviation of field measurements at each site.

Site	Flux μmol m <sup>-2</sup> s <sup>-1</sup>	Soil temp °C	VSWC cm <sup>3</sup> cm <sup>-3</sup>	n
UNDE	2.55 ± 0.26	14.33 ± 0.77	0.33 ± 0.02	61
WOOD	3.02 ± 0.4	16.01 ± 1.54	0.28 ± 0.01	53
WREF	3.62 ± 0.3	15.34 ± 1.76	0.27 ± 0.06	21
KONZ	6.35 ± 0.97	27.28 ± 4.14	0.37 ± 0.01	44
SJER	0.94 ± 0.02	41.68 ± 11.22	0.01 ± 0.01	32
SRER	0.72 ± 0.09	47.64 ± 7.46	0.04 ± 0.01	32

long estimated flux time series and compared those to field measurements made at each site (Figure 5). Results are reported in local time. Where applicable, sites are displayed from left to right by increasing soil temperature (Table 1). Positive values of the flux indicate that there is a flux moving towards the surface. Overall, with the exception of SRER (discussed later) the computed fluxes determined using a variety of plausible methods spanned the field-measured fluxes, but the flux-gradient method that best approximated field measurements varied by site.

### 5.3 Assessment of data gaps

For a given half-hourly time period, the `neonSoilFlux` packages assigns a QA flag for a measurement if more than one values across all measurement depths uses gap-filled data (Section 4.2.1). Panel a of Figure 6 reports the proportion of gap-filled data for all input environmental measurements at each site during the period when field measurements were made. Soil fluxes are computed from 4 different types of input measurements ( $T_S$ ,  $SWC$ ,  $P$ , and CO<sub>2</sub>), any of which could have a QA flag in a half-hourly interval. Panel b of Figure 6 displays at each site the

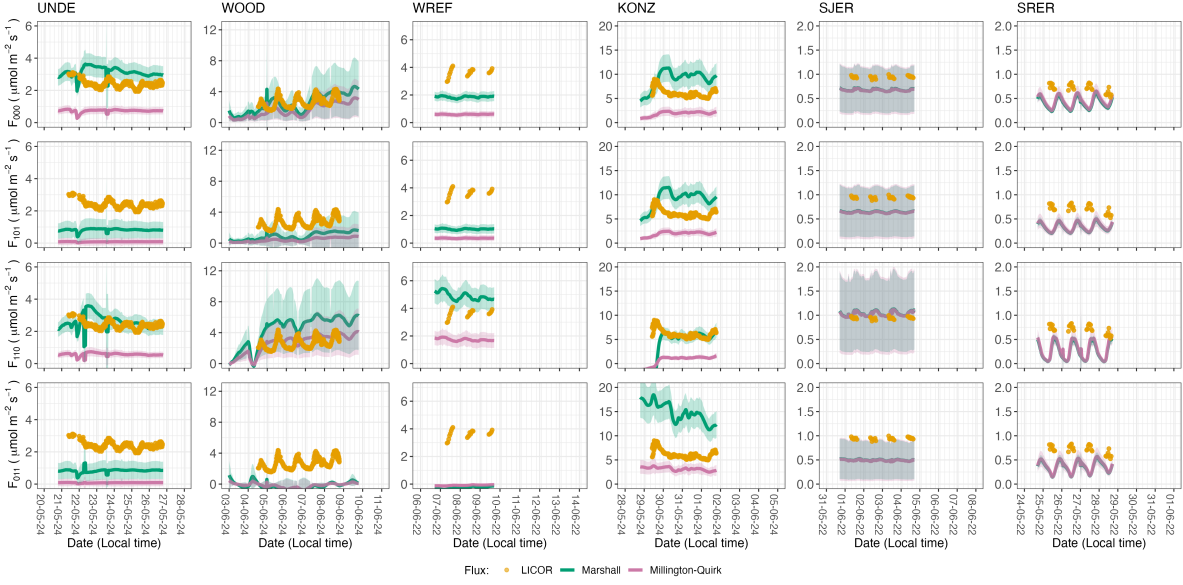


Figure 4: Timeseries of both measured  $F_S$  (yellow circles) and modeled soil fluxes (green or purple lines) by the `neonSoilFlux` R package. Fluxes from the `neonSoilFlux` R package are separated by the diffusivity model used (Millington-Quirk or Marshall, Section 4.2.2). Vertical axis labels in the first column represent the measurement levels where the flux-gradient approach is applied (Section 4.2.3). Ribbons for modeled soil fluxes represent  $\pm 1$  standard deviation. Results are reported in local time.

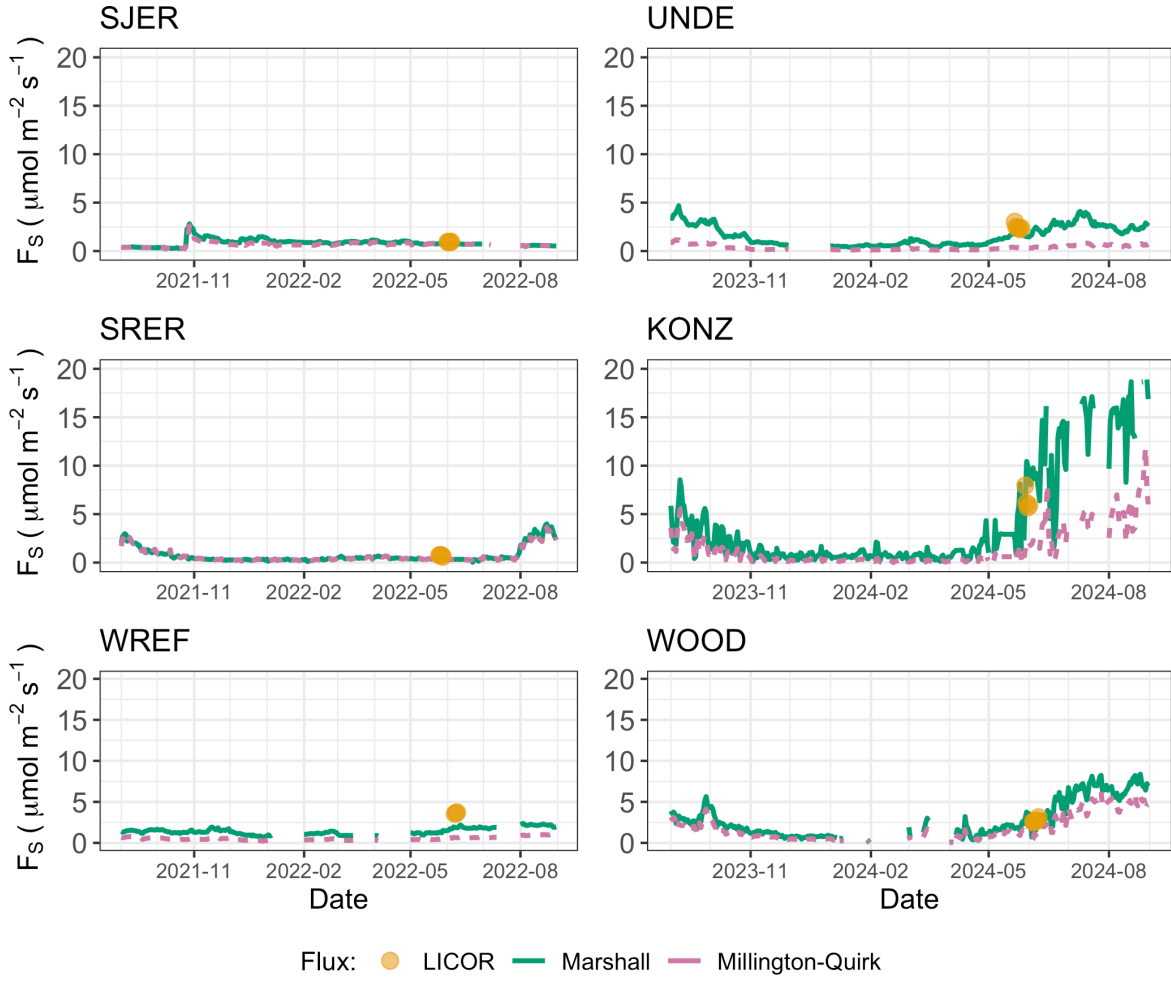


Figure 5: Timeseries of both daily-averaged field  $F_S$  (yellow circles) and daily ensemble averaged soil fluxes (average of  $F_{000}$ ,  $F_{101}$ ,  $F_{011}$ ,  $F_{110}$ , Section 4.2.3) by the `neonSoilFlux` R package, separated by the diffusivity model used (green or purple lines, Millington-Quirk or Marshall, Section 4.2.2).

321 distribution of the number of different gap-filled measurements used to compute a half-hourly  
 322 flux. The largest cause of measurements needing to be gap-filled was missing or flagged soil  
 323 moisture data. SJER and WOOD required the largest number of gap-filled measurements,  
 324 which were primarily  $SWC$  and  $T_S$ .

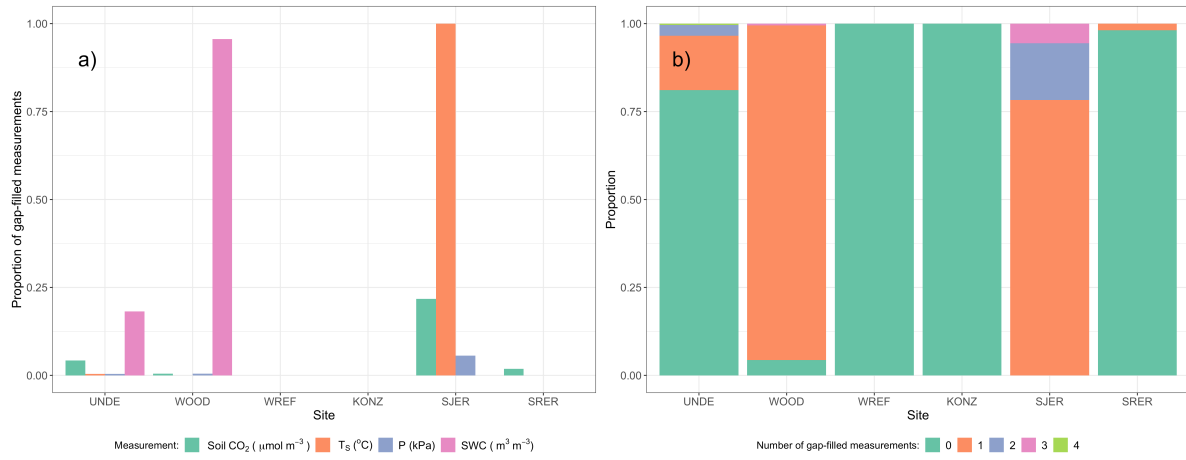


Figure 6: Panel a) Proportion of input gap-filled environmental measurements used to generate  $F_S$  from the `neonSoilFlux` package, by study site. Panel b) distribution of the usage of gap-filled measurements at each site.

## 325 5.4 Assessing the signal to noise ratio (SNR) and evaluating estimated 326 uncertainties

327 The computed signal to noise ratio (SNR) and the proportion of measured field fluxes within  
 328 the modeled uncertainty for a given flux computation method  $F_{ijk}$  suggest that there was  
 329 substantial variability in the agreement between the gradient method and field-measured ob-  
 330 servations (Figure 7, Section 4.3). Here, values of SNR greater than unity indicates lower  
 331 reported uncertainty, as propagated by quadrature due to a relatively higher precision of  
 332 measured input variables ( $\text{CO}_2$ ,  $T_S$ ,  $SWC$ , or  $P$ ).

333 The sensitivity to an uncertainty reduction factor ( $\epsilon$ , bottom panels in Figure 7) demonstrates

334 how concordance between measured and modeled fluxes would be affected if modeled uncer-  
 335 tainty  $\sigma_{ijk}$  decreases. As  $\epsilon$  increases from left to right in each figure, the possible range of  
 336 values for each predicted flux value decreases and the proportion of measured fluxes that fall  
 337 within that range also decreases.

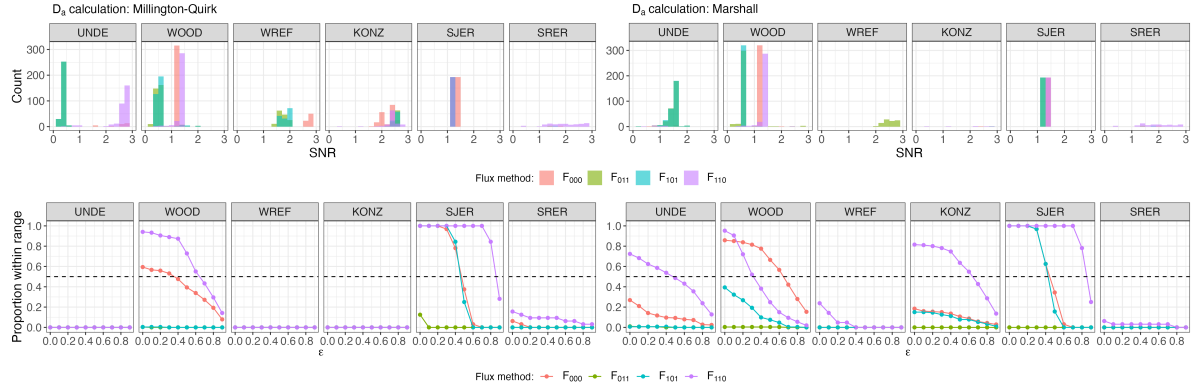


Figure 7: Top panels: distribution of SNR values across each of the different sites for modeled effluxes from the `neonSoilFlux` package, depending on the diffusivity calculation used (Millington-Quirk or Marshall, Section 4.2.2). Bottom panels: Proportion of measured  $F_S$  within the modeled range of a flux computation method  $F_{ijk}$  given an uncertainty reduction factor  $\epsilon$ , or  $|F_S - F_{ijk}| < (1 - \epsilon)\sigma_{ijk}$ .

## 338 5.5 Effects of method choice on diffusivity estimates

339 Figure 8 reports the distribution of  $D_a$  (from both the Marshall and Millington-Quirk methods,  
 340 Section 4.2.2) at each study site, and the *post hoc* computation of  $D_a$  (Section 4.2.2). Over  
 341 the course of a half-hourly interval the same CO<sub>2</sub> gradient (from `neonSoilFlux`) was used for  
 342 the different LICOR measured fluxes. We only used  $F_S$  measured by the LICOR 6800 at all  
 343 sites to standardize comparisons. For the field-estimated measurements we omitted negative  
 344 values of  $D_a$ , as that indicates the CO<sub>2</sub> gradient decreases with soil depth (thereby violating  
 345 assumptions of the flux-gradient method).

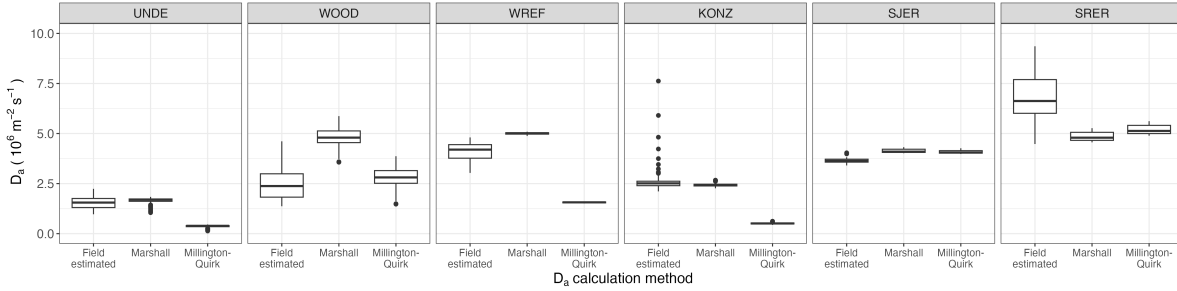


Figure 8: Distribution of diffusivity ( $D_a$ ) at each study site. Values of  $D_a$  were provided by the `neonSoilFlux` package, computed from the Millington-Quirk or Marshall models (Section 4.2.2). A post-hoc estimate of diffusivity (labeled as “Field estimated”) was computed through the field measured flux (Figure 4), divided by the  $\text{CO}_2$  gradient from the measurement levels closest to the soil surface, as reported by NEON.

## 6 Discussion

This study presents a unified data science workflow to efficiently process automated measurements of belowground soil  $\text{CO}_2$  concentrations, water, and temperature to infer estimates of soil surface  $\text{CO}_2$  effluxes through application of Fick’s Law (Equation 4). Our core goals in this study were: (1) to generate estimates of soil flux from continuous soil sensor data at terrestrial NEON sites using the flux-gradient method and then (2) to compare those estimates to field-measured fluxes based on the closed chamber approach at six NEON focal sites. We discuss our progress toward these core goals through (1) an overall evaluation of the flux-gradient approach (and uncertainty calculation) and (2) site-specific evaluation of differences in estimated vs measured fluxes.

### 6.1 General evaluation of flux-gradient approach

Key assumptions of the flux-gradient approach are that  $\text{CO}_2$  concentrations increase throughout the soil profile. Periods where this gradient condition are not met generally are connected

359 to biophysical processes such soil wetting events (e.g. KONZ), which have the effect of reduc-  
360 ing the soil respiration or efflux due to a temporary reduction in diffusivity. When modeling  
361 soil respiration, typically a non-linear response function that also considers soil type is used  
362 (Bouma & Bryla, 2000; Yan et al., 2016, 2018). For the `neonSoilFlux` package, soil type is  
363 connected to the bulk density, which was characterized at each NEON site based on replicate  
364 samples collected from the site megapit at a subset of soil horizons, with an estimated un-  
365 certainty of  $\pm 5\%$  (see NEON User Guide to Soil physical and chemical properties, Megapit  
366 (DP1.00096.001)). Coarse fragment estimates also have very large uncertainties, but because  
367 the volume fraction tends to be low in surface soils it probably wouldn't contribute much  
368 additional flux uncertainty.

369 The largest source of uncertainty to improve reliability of the flux estimate is to prevent the  
370 usage of gap-filled data. Three sites (KONZ, SRER, and KONZ) had more than 75% of half-  
371 hourly periods with no-gap filled measurements. Two sites (SJER and WOOD) had more  
372 than 75% of half-hourly intervals with just one gap-filled measurement. While WREF re-  
373 ported no gap-filled measurements, field data collection occurred following a once-in-a century  
374 rainstorm with soils observed at their water holding capacity. We recommend that whenever  
375 available, local field knowledge is supplementary to any QA filtering protocol of fluxes from  
376 the `neonSoilFlux` package.

377 We recognize that this gap-filling approach may lead to gap-filled values that are quite different  
378 from the actual values, such as an underestimate of soil moisture following rain events. Further  
379 extensions of the gap filling method could use more sophisticated gap-filling routines, similar to  
380 what is used for net ecosystem carbon exchange (Falge et al., 2001; Liu et al., 2023; Mariethoz  
381 et al., 2015; Moffat et al., 2007; Zhang et al., 2023). The current gap-filling routine provides  
382 a consistent approach that can be applied to each data stream, but further work may explore  
383 alternative gap-filling approaches.

384 Based on this approach, we would *a priori* expect  $F_{011} \leq F_{101} \leq F_{110} \leq F_{000}$  because the  
385 previous flux estimates ones correspond to deeper depths which will could miss CO<sub>2</sub> produced  
386 in shallower layers. Additionally, field flux measurements should correlate with  $F_{000}$  because  
387 they represent surface fluxes.

388 **6.2 Evaluation of flux-gradient approach at each site**

389 Derived results from the `neonSoilFlux` package have patterns that are consistent, and com-  
390 parable, to those directly measured to the field (Figure 4 and Figure 5). The advantage to  
391 the `neonSoilFlux` package is the calculation of fluxes across different measurement depths, al-  
392 lowing for additional site-specific customization. Here application of the flux-gradient method  
393 provides a baseline estimate of soil fluxes that could be complemented through additional field  
394 measurements (e.g. LICOR).

395 The six sites studied provide separate case studies for considerations when applying the flux-  
396 gradient method to evaluate resulting uncertainties and fluxes For example, SRER is charac-  
397 terized by sandy soil, which also led to the highest observed field soil temperatures. At SRER  
398 the flux across the top two layers ( $F_{110}$ ) produced a pattern of soil flux consistent with the ob-  
399 served field data. The remaining methods  $F_{101}$ ,  $F_{011}$ , or  $F_{000}$  are derived from information at  
400 the deeper layer, which is decoupled both in terms of temperature and CO<sub>2</sub> concentration.

401 In addition, KONZ is a site that experienced a significant rain event prior to sampling with  
402 eventual drying out over the course of the experiment. In this case we observed storage of soil  
403 water which increased the soil CO<sub>2</sub> at the top layer, leading to negative values of flux at the  
404 start of the experiment, with the fluxes drying out afterwards. In this case only when the soil  
405 dried out (or returned to a baseline level), that the fluxes at the provided layer would work  
406 out in this case.

When considering systematic deployment of this method across a measurement network, we faced a number of independent challenges for consideration. Figure 7 illustrates tradeoffs between (1) accuracy for modeled fluxes (defined here as closeness to field-measured  $F_S$  and the uncertainty reduction factor  $\epsilon$ ), (2) precision (defined by the SNR), and (3) the choice of the diffusivity model (Section 4.2.2) or flux computation method (Section 4.2.3). There was no predictable pattern in SNR for either the flux computation method or diffusivity calculation, indicating that output uncertainty is driven primarily by input measurement uncertainty ( $T_S$ ,  $P$ , SWC, or CO<sub>2</sub>). Across the different flux computation methods, the proportion of measured fluxes where  $|F_S - F_{ijk}| < (1-\epsilon)\sigma_{ijk}$  decreased as  $\epsilon$  increased, except where field  $F_S$  was already outside of the modeled range (i.e. UNDE and WREF). The method  $F_{110}$  (where soil flux was computed from the top two soil layers) was the least sensitive to the uncertainty reduction factor ( $\epsilon$ ). This lack of sensitivity could represent that the LICOR samples from the top surface layer, and is most closely related to assumptions of the  $F_{110}$  method.

Comparing diffusivity methods to field estimated diffusivity (Figure 8) highlights the sensitivity of  $F_{ijk}$  to diffusivity. Site-specific differences reflect the soil moisture availability across the site (Table 1), and also reflect the model variation in Figure 4. While here we compare two approaches to calculated diffusivity (Millington-Quirk or Marshall model), other diffusivity models (e.g. the Moldrup model Moldrup et al. (1999)) could be evaluated. Ultimately the choice of a particular diffusivity model could be determined through site-specific evaluated or a source of model output uncertainty (e.g. as a model ensemble average).

### 6.3 Recommendations for future method development

The neonSoilFlux package provides three different approaches of values for a soil flux. We believe these approaches reflect a variety of site-specific determination and assumptions used to generate a soil flux measurement (Maier & Schack-Kirchner, 2014), with the choice of

431 method having a determinative approach on reported values. Reported results could further  
432 be distilled down using ensemble averaging approaches (Elshall et al., 2018; Raftery  
433 et al., 2005).

434 These challenges notwithstanding, the method used here and made available in the  
435 `neonSoilFlux` R package has the potential to produce nearly continuous estimates of flux  
436 across all terrestrial NEON sites. These estimates are a significant improvement on available  
437 approaches to constrain the portion of ecosystem respiration attributable to the soil. This, in  
438 turn, aids in our ability to understand the components of net ecosystem flux assessed at these  
439 sites using the co-located eddy flux towers.

- 440 • Refine estimates to provide a realistic constraint on surface concentration measurements,  
441 thereby increasing the gradient.
- 442 • Apply machine learning algorithms (e.g. random trees) or model averaging techniques to  
443 generate a single flux estimate across each sites spatial location
- 444 • Benchmarking flux results to estimates provided by net ecosystem carbon exchange.

## 445 7 Conclusions

446 We have here presented an R package `neonSoilFlux` for the estimation of soil CO<sub>2</sub> fluxes from  
447 continuous buried soil sensor measurements across terrestrial National Ecological Observatory  
448 Network sites. We compared the predicted fluxes to those measured directly using a field-based  
449 closed chamber approach. We find that...

450 Baldocchi, D. (2014). Measuring fluxes of trace gases and energy between ecosystems and the  
451 atmosphere - the state and future of the eddy covariance method. *Global Change Biology*,  
452 20(12), 3600–3609. <https://doi.org/10.1111/gcb.12649>

- 453 Berenbaum, M. R., Carpenter, S. R., Hampton, S. E., Running, S. W., & Stanzione, D. C.  
454 (2015). *Report from the NSF BIO Advisory Committee Subcommittee on NEON Scope*  
455 *Impacts*.
- 456 Bond-Lamberty, B. (2018). New Techniques and Data for Understanding the Global Soil Res-  
457piration Flux. *Earth's Future*, 6(9), 1176–1180. <https://doi.org/10.1029/2018EF000866>
- 458 Bond-Lamberty, B., Ballantyne, A., Berryman, E., Fluet-Chouinard, E., Jian, J., Morris, K.  
459 A., Rey, A., & Vargas, R. (2024). Twenty Years of Progress, Challenges, and Opportuni-  
460ties in Measuring and Understanding Soil Respiration. *Journal of Geophysical Research: Bio-geosciences*, 129(2), e2023JG007637. <https://doi.org/10.1029/2023JG007637>
- 461 Bond-Lamberty, B., Christianson, D. S., Malhotra, A., Pennington, S. C., Sihi, D., AghaK-  
462ouchak, A., Anjileli, H., Altaf Arain, M., Armesto, J. J., Ashraf, S., Ataka, M., Baldocchi,  
463 D., Andrew Black, T., Buchmann, N., Carbone, M. S., Chang, S.-C., Crill, P., Curtis, P.  
464 S., Davidson, E. A., ... Zou, J. (2020). COSORE: A community database for continuous  
465 soil respiration and other soil-atmosphere greenhouse gas flux data. *Global Change Biology*,  
466 26(12), 7268–7283. <https://doi.org/10.1111/gcb.15353>
- 467 Bond-Lamberty, B., & Thomson, A. (2010). A global database of soil respiration data. *Bio-  
468geosciences*, 7(6), 1915–1926. <https://doi.org/10.5194/bg-7-1915-2010>
- 469 Bond-Lamberty, B., Wang, C., & Gower, S. T. (2004). A global relationship between the  
470 heterotrophic and autotrophic components of soil respiration? *Global Change Biology*,  
471 10(10), 1756–1766. <https://doi.org/10.1111/j.1365-2486.2004.00816.x>
- 472 Bouma, T. J., & Bryla, D. R. (2000). On the assessment of root and soil respiration for soils  
473 of different textures: Interactions with soil moisture contents and soil CO<sub>2</sub> concentrations.  
474 *Plant and Soil*, 227(1), 215–221. <https://doi.org/10.1023/A:1026502414977>
- 475 Chen, H., & Tian, H.-Q. (2005). Does a General Temperature-Dependent Q10 Model of Soil  
476 Respiration Exist at Biome and Global Scale? *Journal of Integrative Plant Biology*, 47(11),  
477 1288–1302. <https://doi.org/10.1111/j.1744-7909.2005.00211.x>

- 479 Davidson, E. A., Janssens, I. A., & Luo, Y. (2006). On the variability of respiration in  
480 terrestrial ecosystems: Moving beyond Q10. *Global Change Biology*, 12, 154–164. <https://doi.org/10.1111/j.1365-2486.2005.01065.x>
- 482 Desai, A. R., Murphy, B. A., Wiesner, S., Thom, J., Butterworth, B. J., Koupaei-Abyazani, N.,  
483 Muttaqin, A., Paleri, S., Talib, A., Turner, J., Mineau, J., Merrelli, A., Stoy, P., & Davis,  
484 K. (2022). Drivers of Decadal Carbon Fluxes Across Temperate Ecosystems. *Journal of*  
485 *Geophysical Research: Biogeosciences*, 127(12), e2022JG007014. <https://doi.org/10.1029/2022JG007014>
- 487 Elshall, A. S., Ye, M., Pei, Y., Zhang, F., Niu, G.-Y., & Barron-Gafford, G. A. (2018). Relative  
488 model score: A scoring rule for evaluating ensemble simulations with application to micro-  
489 bial soil respiration modeling. *Stochastic Environmental Research and Risk Assessment*,  
490 32(10), 2809–2819. <https://doi.org/10.1007/s00477-018-1592-3>
- 491 Falge, E., Baldocchi, D., Olson, R., Anthoni, P., Aubinet, M., Bernhofer, C., Burba, G.,  
492 Ceulemans, R., Clement, R., Dolman, H., Granier, A., Gross, P., Grünwald, T., Hollinger,  
493 D., Jensen, N.-O., Katul, G., Keronen, P., Kowalski, A., Lai, C. T., ... Wofsy, S. (2001).  
494 Gap filling strategies for defensible annual sums of net ecosystem exchange. *Agricultural*  
495 *and Forest Meteorology*, 107(1), 43–69. [https://doi.org/10.1016/S0168-1923\(00\)00225-2](https://doi.org/10.1016/S0168-1923(00)00225-2)
- 496 Farrance, I., & Frenkel, R. (2012). *Uncertainty of Measurement: A Review of the Rules*  
497 *for Calculating Uncertainty Components through Functional Relationships*. *The Clinical*  
498 *Biochemist Reviews*, 33(2), 49–75.
- 499 Friedlingstein, P., O’Sullivan, M., Jones, M. W., Andrew, R. M., Bakker, D. C. E., Hauck,  
500 J., Landschützer, P., Le Quéré, C., Luijkx, I. T., Peters, G. P., Peters, W., Pongratz, J.,  
501 Schwingshackl, C., Sitch, S., Canadell, J. G., Ciais, P., Jackson, R. B., Alin, S. R., Anthoni,  
502 P., ... Zheng, B. (2023). Global Carbon Budget 2023. *Earth System Science Data*, 15(12),  
503 5301–5369. <https://doi.org/10.5194/essd-15-5301-2023>
- 504 Hamdi, S., Moyano, F., Sall, S., Bernoux, M., & Chevallier, T. (2013). Synthesis analysis

- 505 of the temperature sensitivity of soil respiration from laboratory studies in relation to  
506 incubation methods and soil conditions. *Soil Biology and Biochemistry*, 58, 115–126. <https://doi.org/10.1016/j.soilbio.2012.11.012>
- 507 Hirano, T., Kim, H., & Tanaka, Y. (2003). Long-term half-hourly measurement of soil CO<sub>2</sub>  
508 concentration and soil respiration in a temperate deciduous forest. *Journal of Geophysical  
509 Research: Atmospheres*, 108(D20). <https://doi.org/10.1029/2003JD003766>
- 510 Jackson, R. B., Lajtha, K., Crow, S. E., Hugelius, G., Kramer, M. G., & Piñero, G. (2017).  
511 The Ecology of Soil Carbon: Pools, Vulnerabilities, and Biotic and Abiotic Controls.  
512 *Annual Review of Ecology, Evolution and Systematics*, 48(Volume 48, 2017), 419–445.  
513 <https://doi.org/10.1146/annurev-ecolsys-112414-054234>
- 514 Jian, J., Bailey, V., Dorheim, K., Konings, A. G., Hao, D., Shiklomanov, A. N., Snyder, A.,  
515 Steele, M., Teramoto, M., Vargas, R., & Bond-Lamberty, B. (2022). Historically inconsis-  
516 tent productivity and respiration fluxes in the global terrestrial carbon cycle. *Nature  
517 Communications*, 13(1), 1733. <https://doi.org/10.1038/s41467-022-29391-5>
- 518 Jian, J., Vargas, R., Anderson-Teixeira, K., Stell, E., Herrmann, V., Horn, M., Kholod, N.,  
519 Manzon, J., Marchesi, R., Paredes, D., & Bond-Lamberty, B. (2021). A restructured and  
520 updated global soil respiration database (SRDB-V5). *Earth System Science Data*, 13(2),  
521 255–267. <https://doi.org/10.5194/essd-13-255-2021>
- 522 Jiang, J., Feng, L., Hu, J., Liu, H., Zhu, C., Chen, B., & Chen, T. (2024). Global soil  
523 respiration predictions with associated uncertainties from different spatio-temporal data  
524 subsets. *Ecological Informatics*, 82, 102777. <https://doi.org/10.1016/j.ecoinf.2024.102777>
- 525 Jobbágy, E. G., & Jackson, R. B. (2000). The Vertical Distribution of Soil Organic Carbon  
526 and its Relation to Climate and Vegetation. *Ecological Applications*, 10(2), 423–436. [https://doi.org/10.1890/1051-0761\(2000\)010%5B0423:TVDOSO%5D2.0.CO;2](https://doi.org/10.1890/1051-0761(2000)010%5B0423:TVDOSO%5D2.0.CO;2)
- 527 Liu, K., Li, X., Wang, S., & Zhang, H. (2023). A robust gap-filling approach for European  
528 Space Agency Climate Change Initiative (ESA CCI) soil moisture integrating satellite
- 529

- 531 observations, model-driven knowledge, and spatiotemporal machine learning. *Hydrology*  
532 and *Earth System Sciences*, 27(2), 577–598. <https://doi.org/10.5194/hess-27-577-2023>
- 533 Luo, Y., Ogle, K., Tucker, C., Fei, S., Gao, C., LaDeau, S., Clark, J. S., & Schimel, D. S. (2011).  
534 Ecological forecasting and data assimilation in a data-rich era. *Ecological Applications*,  
535 21(5), 1429–1442. <https://doi.org/10.1890/09-1275.1>
- 536 Maier, M., & Schack-Kirchner, H. (2014). Using the gradient method to determine soil gas  
537 flux: A review. *Agricultural and Forest Meteorology*, 192–193, 78–95. <https://doi.org/10.1016/j.agrformet.2014.03.006>
- 538 Mariethoz, G., Linde, N., Jougnot, D., & Rezaee, H. (2015). Feature-preserving interpolation  
539 and filtering of environmental time series. *Environmental Modelling & Software*, 72, 71–76.  
540 <https://doi.org/10.1016/j.envsoft.2015.07.001>
- 541 Marshall, T. J. (1959). The Diffusion of Gases Through Porous Media. *Journal of Soil Science*,  
542 10(1), 79–82. <https://doi.org/10.1111/j.1365-2389.1959.tb00667.x>
- 543 Millington, R. J., & Shearer, R. C. (1971). Diffusion in aggregated porous media. *Soil Science*,  
544 111(6), 372–378.
- 545 Moffat, A. M., Papale, D., Reichstein, M., Hollinger, D. Y., Richardson, A. D., Barr, A. G.,  
546 Beckstein, C., Braswell, B. H., Churkina, G., Desai, A. R., Falge, E., Gove, J. H., Heimann,  
547 M., Hui, D., Jarvis, A. J., Kattge, J., Noormets, A., & Stauch, V. J. (2007). Comprehensive  
548 comparison of gap-filling techniques for eddy covariance net carbon fluxes. *Agricultural and  
549 Forest Meteorology*, 147(3), 209–232. <https://doi.org/10.1016/j.agrformet.2007.08.011>
- 550 Moldrup, P., Olesen, T., Yamaguchi, T., Schjønning, P., & Rolston, D. E. (1999). Modeling  
551 diffusion and reaction in soils: 9. The Buckingham-Burdine-Campbell equation for gas  
552 diffusivity in undisturbed soil. *Soil Science*, 164(2), 75.
- 553 National Ecological Observatory Network (NEON). (2024a). *Barometric pressure*  
554 (*DP1.00004.001*). National Ecological Observatory Network (NEON). <https://doi.org/10.48443/RT4V-KZ04>

- 557 National Ecological Observatory Network (NEON). (2024b). *Soil CO<sub>2</sub> concentration (DP1.00095.001)*. National Ecological Observatory Network (NEON). <https://doi.org/10.48443/E7GR-6G94>
- 560 National Ecological Observatory Network (NEON). (2024c). *Soil physical and chemical properties, Megapit (DP1.00096.001)*. National Ecological Observatory Network (NEON). <https://doi.org/10.48443/S6ND-Q840>
- 563 National Ecological Observatory Network (NEON). (2024d). *Soil temperature (DP1.00041.001)*. National Ecological Observatory Network (NEON). <https://doi.org/10.48443/Q24X-PW21>
- 565 National Ecological Observatory Network (NEON). (2024e). *Soil water content and water salinity (DP1.00094.001)*. National Ecological Observatory Network (NEON). <https://doi.org/10.48443/A8VY-Y813>
- 568 Norman, J. M., Kucharik, C. J., Gower, S. T., Baldocchi, D. D., Crill, P. M., Rayment, M., Savage, K., & Striegl, R. G. (1997). A comparison of six methods for measuring soil-surface carbon dioxide fluxes. *Journal of Geophysical Research: Atmospheres*, 102(D24), 28771–28777. <https://doi.org/10.1029/97JD01440>
- 572 Phillips, C. L., Bond-Lamberty, B., Desai, A. R., Lavoie, M., Risk, D., Tang, J., Todd-Brown, K., & Vargas, R. (2017). The value of soil respiration measurements for interpreting and modeling terrestrial carbon cycling. *Plant and Soil*, 413(1), 1–25. <https://doi.org/10.1007/s11104-016-3084-x>
- 576 Raftery, A. E., Gneiting, T., Balabdaoui, F., & Polakowski, M. (2005). *Using Bayesian Model Averaging to Calibrate Forecast Ensembles*. <https://doi.org/10.1175/MWR2906.1>
- 580 Sallam, A., Jury, W. A., & Letey, J. (1984). Measurement of Gas Diffusion Coefficient under Relatively Low Air-filled Porosity. *Soil Science Society of America Journal*, 48(1), 3–6. <https://doi.org/10.2136/sssaj1984.03615995004800010001x>
- 581 Shao, J., Zhou, X., Luo, Y., Li, B., Aurela, M., Billesbach, D., Blanken, P. D., Bracho, R., Chen, J., Fischer, M., Fu, Y., Gu, L., Han, S., He, Y., Kolb, T., Li, Y., Nagy, Z., Niu, S.,

- 583 Oechel, W. C., ... Zhang, J. (2015). Biotic and climatic controls on interannual variability  
584 in carbon fluxes across terrestrial ecosystems. *Agricultural and Forest Meteorology*, 205,  
585 11–22. <https://doi.org/10.1016/j.agrformet.2015.02.007>
- 586 Shao, P., Zeng, X., Moore, D. J. P., & Zeng, X. (2013). Soil microbial respiration from  
587 observations and Earth System Models. *Environmental Research Letters*, 8(3), 034034.  
588 <https://doi.org/10.1088/1748-9326/8/3/034034>
- 589 Sihi, D., Gerber, S., Inglett, P. W., & Inglett, K. S. (2016). Comparing models of microbial–  
590 substrate interactions and their response to warming. *Biogeosciences*, 13(6), 1733–1752.  
591 <https://doi.org/10.5194/bg-13-1733-2016>
- 592 Tang, J., Baldocchi, D. D., Qi, Y., & Xu, L. (2003). Assessing soil CO<sub>2</sub> efflux using continuous  
593 measurements of CO<sub>2</sub> profiles in soils with small solid-state sensors. *Agricultural and Forest  
594 Meteorology*, 118(3), 207–220. [https://doi.org/10.1016/S0168-1923\(03\)00112-6](https://doi.org/10.1016/S0168-1923(03)00112-6)
- 595 Tang, J., Misson, L., Gershenson, A., Cheng, W., & Goldstein, A. H. (2005). Continuous  
596 measurements of soil respiration with and without roots in a ponderosa pine plantation  
597 in the Sierra Nevada Mountains. *Agricultural and Forest Meteorology*, 132(3), 212–227.  
598 <https://doi.org/10.1016/j.agrformet.2005.07.011>
- 599 Taylor, J. R. (2022). *An Introduction to Error Analysis: The Study of Uncertainties in Physical  
600 Measurements, Third Edition* (3rd ed.). University Science Press.
- 601 Yan, Z., Bond-Lamberty, B., Todd-Brown, K. E., Bailey, V. L., Li, S., Liu, C., & Liu, C. (2018).  
602 A moisture function of soil heterotrophic respiration that incorporates microscale processes.  
603 *Nature Communications*, 9(1), 2562. <https://doi.org/10.1038/s41467-018-04971-6>
- 604 Yan, Z., Liu, C., Todd-Brown, K. E., Liu, Y., Bond-Lamberty, B., & Bailey, V. L. (2016).  
605 Pore-scale investigation on the response of heterotrophic respiration to moisture conditions  
606 in heterogeneous soils. *Biogeochemistry*, 131(1), 121–134. <https://doi.org/10.1007/s10533-016-0270-0>
- 608 Zhang, R., Kim, S., Kim, H., Fang, B., Sharma, A., & Lakshmi, V. (2023). Temporal

609      Gap-Filling of 12-Hourly SMAP Soil Moisture Over the CONUS Using Water Balance  
610      Budgeting. *Water Resources Research*, 59(12), e2023WR034457. <https://doi.org/10.1029/2023WR034457>